PAPER

Check for updates

Fabrication of a CuS-cocatalyst-supported g-C₃N₄ nanosheet composite photocatalyst with improved performance in the photocatalytic reduction of CO₂†

Fangjun Wang,[a] Shiyi Chen,[a] Jiang Wu,*[bc] Wenguo Xiang [ID] [a] and Lunbo Duan [ID] *[a]

Carbon dioxide (CO_2) is not only a greenhouse gas but also an abundant carbon resource. By using solar energy to reduce CO_2 into high-value hydrocarbons *via* photocatalysis, we can mitigate the greenhouse effect and enable energy recycling. In this paper, a two-step calcination process was employed to thermally exfoliate graphite-phase carbon nitride (g-C_3N_4) into ultrathin nanosheets, after which the CuS co-catalyst was loaded onto the g-C_3N_4 surface using a one-step hydrothermal method. The ultrathin nanosheet structure of g-C_3N_4 can increase the specific surface area of the composite material and improve the anchoring of active components and CO_2 adsorption sites. CuS, acting as a co-catalyst, can capture photogenerated electrons from the g-C_3N_4 conduction band, thereby enhancing the separation and migration of photogenerated charges. Moreover, the interfacial charge transfer (IFCT) mechanism of CuS enhances the efficiency of separating photogenerated electrons and holes. The prepared 10CuS/g-C_3N_4 composite photocatalyst, loaded with 10 wt% CuS, has significantly improved CO_2 photoreduction performance. The highest CO yield reached 15.34 μmol g^{-1}. This work provides guidance for developing low-cost artificial photosynthesis to utilize CO_2 as a resource.

1. Introduction

Due to the ongoing energy crisis driven by the excessive reliance on fossil fuels, humanity must urgently seek alternative energy sources. Meanwhile, the burning of fossil fuels has also caused a significant rise in carbon dioxide (CO_2) emissions, contributing to global warming, rising sea levels, and a series of climate-related problems.[1,2] In order to address both the energy crisis and environmental issues, photocatalysis for converting CO_2 into hydrocarbons is considered a highly promising solution.[3,4] Therefore, the development of efficient and stable photocatalysts presents both a significant opportunity and a challenge.

In this context, carbon-based nanomaterials-metal-free, sunlight-activated photoredox catalysts are extensively utilized across diverse fields.[5,6] These include metal-free oxidation/reduction, solar fuel production, light-emitting diodes, bioimaging, sensing, fuel/solar cells, and photoelectric conversion, among others.[7] Their widespread application stems from their unique properties, such as an attractive electronic band structure, compositional versatility, high solar-energy utilization efficiency, stability, ease of fabrication, robust physicochemical stability, and their 'earth-abundant' nature. To date, researchers have investigated a wide range of photocatalysts. Among these catalysts, graphitic carbon nitride (g-C_3N_4), a low-cost non-metallic semiconductor, exhibits great potential for application in the photocatalytic reduction of CO_2 due to its excellent stability and unique energy band structure.[8,9] However, the practical application of bulk g-C_3N_4 is limited by its small specific surface area and high recombination rate of photogenerated carriers.[10–12] Regarding this, various methods have been employed to modify carbon nitride materials, for example, *via* doping elements,[13,14] introducing defects,[15–17] and constructing heterostructures.[18–20]

Under light irradiation, the electrons generated within the semiconductor can be transferred to the co-catalyst, promoting the efficient separation of photogenerated electron–hole pairs.[21–23] Therefore, the loading of co-catalysts is an effective strategy to improving the photoreduction performance of pure g-C_3N_4. The majority of previously reported highly efficient co-catalysts are precious metals, which significantly increases their cost.[24] To better achieve industrial applications, transition metal compounds are regarded as excellent co-catalysts for replacing

[a]Key Laboratory of Energy Thermal Conversion and Control of Ministry of Education, School of Energy and Environment, Southeast University, No. 2 Sipailou, Xuanwu District, Nanjing 210096, China. E-mail: duanlunbo@seu.edu.cn; Tel: +86-13951912858

[b]College of Energy and Mechanical Engineering, Shanghai University of Electric Power, No. 2103 Pingliang Road, Shanghai 200090, China. E-mail: wjcfd2002@163.com; Tel: +86-21-35303902; +86-13371896217

[c]Shanghai Institute of Pollution Control and Ecological Security, Shanghai, China

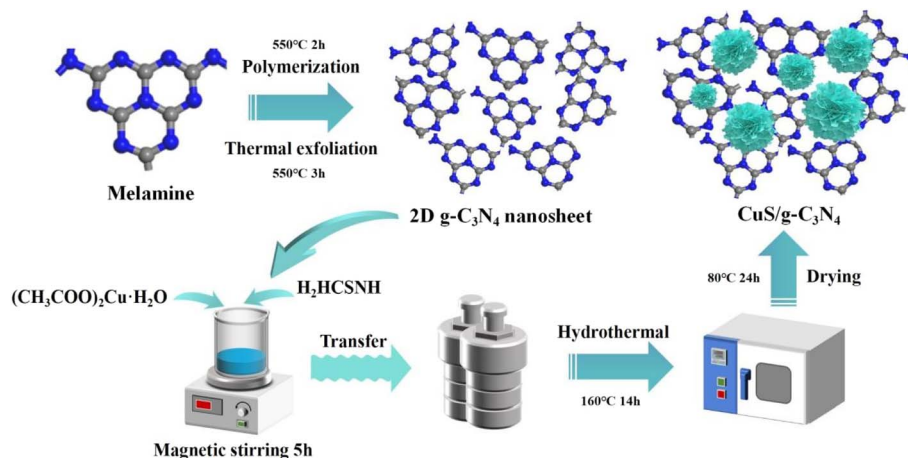† Electronic supplementary information (ESI) available. See DOI: https://doi.org/10.1039/d5ra02234g

Fig. 1 Flowchart for the preparation of CuS/CN.

precious metals.[25,26] Zheng *et al.* developed an Mo–Mo$_2$C co-catalyst, and experimental results demonstrated its efficiency in suppressing photogenerated charge recombination, thereby enhancing interfacial charge transfer.[27] Lu *et al.* demonstrated that the non-noble metal Ni$_3$B/Ni(OH)$_2$ significantly enhances the photocatalytic H$_2$ production efficiency of g-C$_3$N$_4$.[28]

Copper, an abundant and cost-effective transition metal, is considered as an effective co-catalyst for the photocatalytic reduction of CO$_2$.[29] Currently, various copper-based co-catalysts have been synthesized. Yin *et al.* deposited amorphous CuO nanoclusters onto niobate nanosheets. The electron spin resonance (ESR) analysis indicates that photogenerated electrons in the conduction band (CB) of niobate nanosheets are transferred to CuO nanoclusters *via* the interface, where they engage in the CO$_2$ photoreduction reaction.[30] Meanwhile, this further confirms that electrons in the valence band (VB) of the semiconductor can migrate to the Cu-based co-catalyst *via* direct photoinduced interfacial charge transfer (IFCT). In this process, the Cu-based co-catalyst functions as an electron acceptor, facilitating the separation of photogenerated charges. Zhang *et al.* used CuS as a co-catalyst to dope ZnS nanosheets and confirmed that CuS directly accepts electrons transferred from the VB of ZnS. Without the addition of any precious metals, the hydrogen production rate of the CuS/ZnS composite catalyst reached 4147 μmol g^{-1} h^{-1}.[31] On the other hand, the S element in CuS can effectively limit the rapid recombination of carriers. Arumugam *et al.* studied the effect of several non-metal element doping on the photocatalytic performance of g-C$_3$N$_4$. They found that carbon nitride doped with S element had the best CH$_4$ yield.[32]

In this paper, the CO$_2$ photoreduction performance of g-C$_3$N$_4$ was enhanced through carbon nitride morphology regulation and the incorporation of a CuS co-catalyst. Bulk g-C$_3$N$_4$ was thermally exfoliated into ultrathin g-C$_3$N$_4$ nanosheets, increasing the surface area of the photocatalyst, while the incorporation of a CuS co-catalyst facilitated the separation and transfer of photogenerated charges. In compared to pure g-C$_3$N$_4$, the CuS/g-C$_3$N$_4$ composite demonstrates superior photocatalytic performance, with a CO yield 1.9 times that of g-C$_3$N$_4$. In addition, this work proposes the IFCT mechanism to further

elucidate the photogenerated electron transfer pathway. The research results offer new possibilities for the development of efficient, low-cost, non-precious metal photocatalysts.

2. Experimental section

The characterization and photocatalytic activity experiments conducted in this study are detailed in the ESI.†

2.1 Materials

Melamine (C$_3$H$_6$N$_6$), thiourea (H$_2$NCSNH$_2$) and copper (II) acetate monohydrate ((CH$_3$COO)$_2$Cu·H$_2$O) were all provided Sinopharm Chemical Reagent Corp. All the chemicals were of analytical grade and could be used without further purification. Deionized water and absolute ethanol were used for washing and as solvents throughout the experiments.

2.2 Catalyst preparation

In this experiment, a two-step calcination process was employed to prepare g-C$_3$N$_4$ nanosheets, and a hydrothermal method was employed to synthesize the CuS/g-C$_3$N$_4$ composite photocatalyst. The specific process is as follows.

2.2.1 Preparation of g-C$_3$N$_4$ nanosheet (CN). The ultrathin 2D g-C$_3$N$_4$ nanosheets were synthesized using a typical two-step calcination method.[33] First, 10.0 g of C$_3$H$_6$N$_6$ was placed in a covered crucible, heated to 550 °C in air, and then held at 550 °C for 2 hours. The obtained yellow block solid was ground into a 80–120 mesh powder. Then, 5.0 g of the ground powder was evenly spread in an uncovered porcelain boat, heated to 550 °C, and calcined for 3 hours. After natural cooling, the light yellow powder obtained was g-C$_3$N$_4$ nanosheets, labeled as CN.

2.2.2 Preparation of CuS/g-C$_3$N$_4$ (CuS/CN). The CuS/g-C$_3$N$_4$ composite photocatalyst was synthesized using a one-step hydrothermal method, as illustrated in Fig. 1.[34] First, the previously prepared g-C$_3$N$_4$ nanosheets were dispersed in 50 mL of deionized water by ultrasonication for 0.5 hours, and then 0.116 g of (CH$_3$COO)$_2$Cu·H$_2$O was dissolved in the solution. Dissolve 0.044 g H$_2$NCSNH$_2$ in 40 mL deionized water and drip it into the above suspension while stirring vigorously. Finally,

the uniformly mixed solution was placed in an autoclave and hydrothermally heated at 160 °C for 14 hours. After cooling naturally, the product was washed three times, and the precipitate was collected by centrifugation and dried in an oven at 80 °C for 24 hours. The photocatalyst prepared by the above steps is denoted as 10CuS/CN. By varying the amount of $(CH_3COO)_2Cu \cdot H_2O$ and H_2NCSNH_2, the same steps were followed to prepare different percentages of xCuS/CN (x = 5, 10, 15 and 20 wt%) composite photocatalysts.

3. Results and discussion

3.1 XRD and FTIR analysis

The crystal phases of all catalysts were characterized by XRD, as shown in Fig. 2(a). The diffraction peaks observed at 2theta values of 27.7°, 29.2°, 31.8°, 32.8°, 47.9°, and 59.3° belong to the (1 0 1), (1 0 2), (1 0 3), (0 0 6), (1 1 0), and (1 1 6) crystal planes of CuS (JCPDS No. 06-0464).[35,36] The g-C_3N_4 shows a distinct peak around 27.5°, which can be indexed to the (0 0 2) crystal plane of CN.[37] The distinct and intense peaks suggest that the prepared catalyst possesses good crystallinity, and the as-synthesized CuS and g-C_3N_4 show no additional impurity peaks, implying that they exist as pure substances. In the CuS/CN composite photocatalyst, when the CuS content is 5 wt%, the peak of CuS is barely visible, possibly due to the CuS content being too low or CuS existing in an amorphous phase on the CN surface. It is noteworthy that in all CuS/CN composites, the (0 0 2) diffraction peak of CN shifts to higher 2theta values. This change may be due to the electronic effects caused by the well-dispersed Cu atoms on the surface of CN nanosheets, indicating the formation of a heterojunction between CuS and CN. As the CuS content increases, the typical diffraction peak of g-C_3N_4 gradually weakens, while the diffraction peak of CuS became stronger. Therefore, the XRD results validate the successful synthesis of the CuS/CN composite photocatalyst. Furthermore, the functional groups in the composites were analyzed by FTIR.

The FTIR spectra of CuS/CN composites and the CN were recorded in the range of 500–3500 cm^{-1} (Fig. 2(b)). The characteristic signal at 810 cm^{-1} for all samples is assigned to the stretching vibration of the triazine units in the molecules.[38] Furthermore, the absorptions at 1245 cm^{-1}, 1275 cm^{-1}, 1374 cm^{-1}, 1510 cm^{-1}, and 1655 cm^{-1} are attributed to the characteristic stretching modes of the aromatic C–N and C=N heterocyclic systems.[39,40] The broad absorption band at 3200 cm^{-1} corresponds to the typical N–H and O–H stretching vibrations.[41] The FTIR spectrum shows that after CuS is loaded onto CN, the absorption band of the composite photocatalyst does not change significantly, suggesting that the incorporation of CuS does not destroy the structural integrity of CN, which aligns with the XRD analysis results.

3.2 XPS analysis

To analyze the elemental composition and chemical state of the composite photocatalyst, 10CuS/CN was characterized by XPS. The full XPS in Fig. 3(a) reveals the presence of C, N, O, Cu, and S in the 10CuS/CN sample, once again confirming the successful synthesis of the composite photocatalyst. Among them, the characteristic signal of O 1s primarily comes from the oxygen adsorbed from the air. Fig. 3(b)–(e) shows the high-resolution XPS spectra of the elements in the samples. As can be seen from Fig. 3(b), the C 1s can be deconvoluted into two main characteristic signals. The peak at 289.0 eV is associated with the N–C=N functional group, whereas the peak at 286.1 eV is linked to the C–$(N)_3$ structure.[42] The N 1s spectrum in Fig. 3(c) can be deconvoluted into three peaks. The peak at 401.6 eV is associated with the amino group (–NH_2), and the peak at 400.0 eV can be attributed to the tertiary nitrogen (N–$(C)_3$) of g-C_3N_4. The peak at 399.4 eV is assigned to sp^2-hybridized nitrogen (N–C=N), indicating the presence of sp^2-bonded graphitic carbon nitride.[43] The binding energies of Cu $2p_{3/2}$ and Cu $2p_{1/2}$ in Fig. 3(d) are located at 935.9 eV and 952.6 eV, respectively, which are characteristic of Cu^{2+} in CuS, while the peak at 933.1 eV corresponds to Cu^+. The binding energy of Cu 2p in the CuS/CN prepared in this work are slightly higher than the values of 932.1 eV and 952.0 eV reported in previous literature.[44,45] This change is primarily due to the different electron concentrations caused by the charge transfer and interfacial interactions between CuS and CN. We speculate that
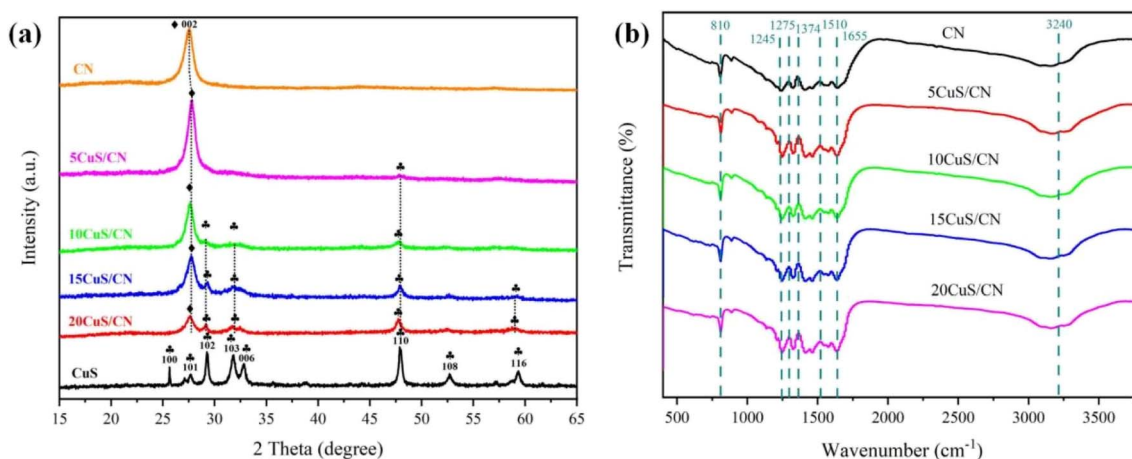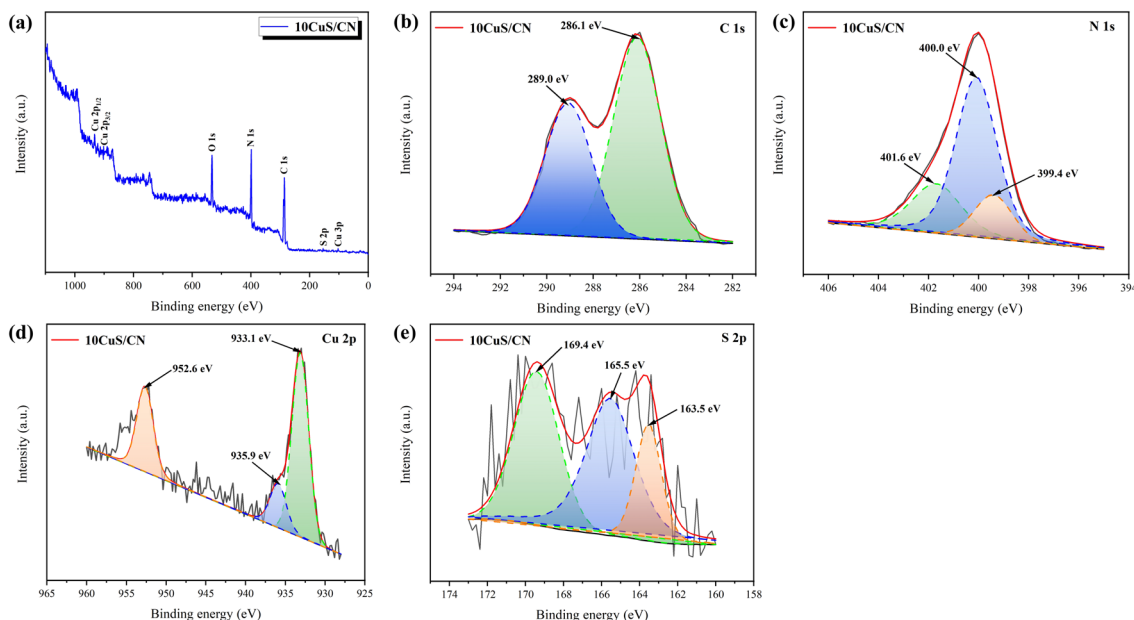

Fig. 2 (a) XRD and (b) FTIR spectra of CN, and CuS/CN.

Fig. 3 (a) Full XPS spectrum of the prepared 10CuS/CN; (b) high-resolution XPS spectra of C 1s, (c) N 1s, (d) S 2p, and (e) Cu 2p.

a heterojunction may form between CuS and CN and have a synergistic effect, which is beneficial to the separation and transport of charge carriers, thereby enhancing the performance of the composite photocatalyst. The XRD and FTIR analysis results above also show that there is not only a physical interaction but also chemical interaction between CuS and CN. The S 2p XPS in Fig. 3(e) can be divided into three characteristic peaks. The peak at 169.4 eV corresponds to sulfate (SO_4^{2-}), which may originate from the oxidation of certain sulfur species on the surface by atmospheric oxygen. The characteristic peaks at 165.5 eV and 163.5 eV are attributed to polysulfide (S_x^{2-}) and sulfides (S^{2-}), respectively.[46]

3.3 SEM, TEM and TEM-EDS analysis

The morphological of the prepared CN and CuS/CN composites were observed using SEM and TEM. As shown in Fig. 4(a), CN forms an agglomerate consisting of curled sheet-like structures, with pore structures distributed across the surface. After the introduction of CuS (Fig. 4(b)), CuS particles appeared on CN, and the CuS/CN exhibited slight agglomeration, which may lead to changes in the composite's specific surface area. Fig. 4(c) shows the TEM image of CN, revealing a highly transparent features that indicates its ultra-thin characteristics. In addition, as shown in Fig. 4(d), CuS particles (black dots within the yellow circle) are clearly visible on the CN surface. No significant aggregates are observed, and the CuS particles are evenly distributed over the CN. The microstructures of CN and 10CuS/CN were further observed using HR-TEM. As can be seen from Fig. 4(e), there are no obvious lattice fringes in the CN, indicating that CN is an amorphous nanosheet.[47] In the HR-TEM image of the 10CuS/CN composite shown in Fig. 4(f), the CuS lattice fringes are clearly visible, with lattice spacings of 0.218 nm and 0.305 nm corresponding to the (1 0 5) and (1 0 2) crystal planes of CuS, respectively.[48] Meanwhile, the contact boundary between CuS and CN is visible, and the close

interaction between CuS and CN nanosheets facilitates charge transfer, thereby enhancing photocatalytic activity.

To further verify the good dispersion of CuS on CN nanosheets, elemental mapping of the 10CuS/CN sample was performed, and the results are presented in Fig. 5(a). The results show that the Cu, S, C, and N elements are evenly distributed in the composite material without obvious agglomeration. The selected area electron diffraction (SAED) in Fig. 5(b) shows diffuse Debye–Scherrer rings, indicating the polycrystalline nature of the heterojunction, corresponding to the (1 0 2) crystal plane of hexagonal CuS (JCPDS No. 06-0464) and CN, respectively, which is consistent with the XRD in Fig. 2(a). EDS analysis was performed on area #1 shown in Fig. 5(c) to determine the elements present in the catalyst and their respective percentages. Fig. 5(d) shows the TEM-EDS spectrum, which clearly demonstrates the presence of Cu, S, C, and N in the 10CuS/CN, as well as their respective percentages in the composite. The content of CuS in the energy spectrum is generally consistent with the actual composition of CuS on CN. The above analysis indicate that all elements are well distributed throughout the composite material, and the element proportions align with expectations, confirming the successful preparation of CuS-doped CN nanosheet photocatalysts.

3.4 BET surface area and pore size distribution analysis

The structural properties of CuS, CN, and all CuS/CN composites were analyzed using the nitrogen adsorption–desorption method. Fig. 6(a) demonstrates that all samples display type IV isotherms with H3-type hysteresis loops at higher pressures. According to the IUPAC classification,[49] the composite material has a mesoporous structure. In addition, as seen in the pore size distribution graph in Fig. 6(b), the pore size distribution of all samples is primarily concentrated within the range of 2.9–19.1 nm, which further confirms the existence of mesopores.
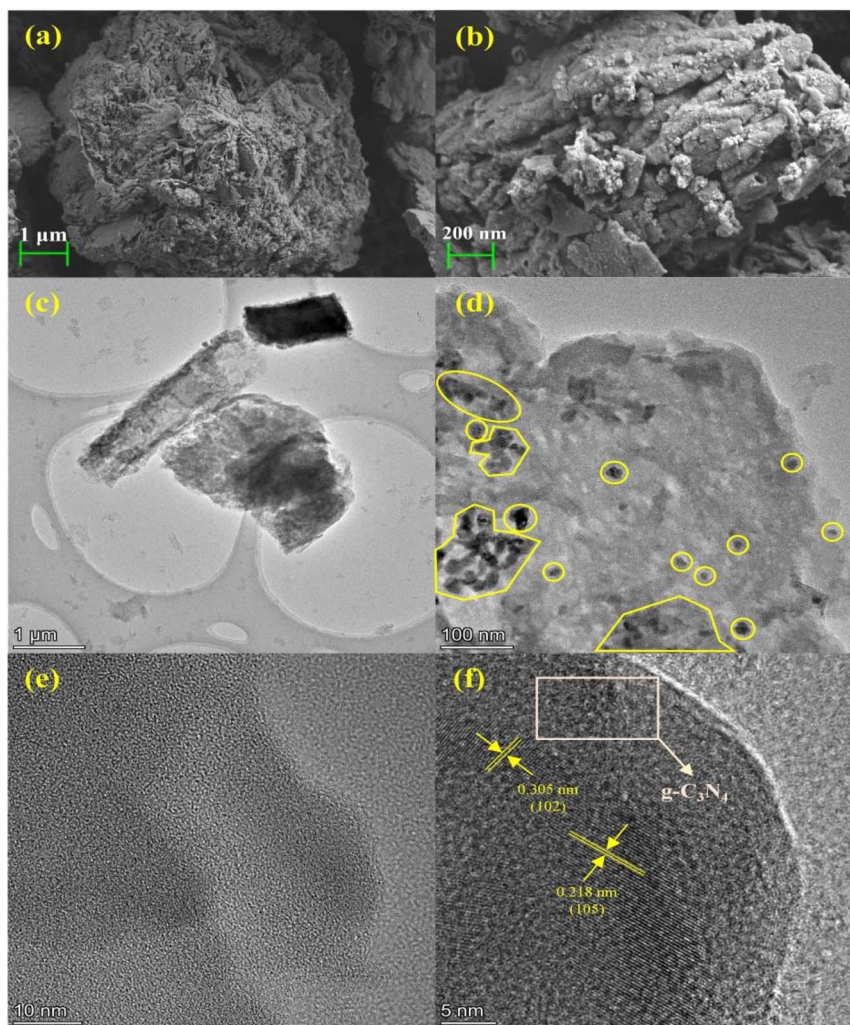
Fig. 4 (a) SEM images, (c) TEM images, (e) HRTEM of CN; (b) SEM images, (d) TEM images, (f) HRTEM of 10CuS/CN.

The BET surface area, pore volume, and pore size of CuS, CN, and CuS/CN composites with different CuS doping ratios are summarized in Table 1. In general, photocatalysts with a larger specific surface area and suitable pore size facilitate the adsorption and diffusion of CO_2, thereby promoting effective photocatalytic reduction of CO_2. The BET surface areas of CuS and CN are 7.4123 m^2 g^{-1} and 50.7652 m^2 g^{-1}, respectively. Compared with pure CuS and CN, the BET surface area of the CuS/CN composites increased, with 10CuS/CN exhibiting the largest surface area of 66.8470 m^2 g^{-1}. However, with the continued increase in CuS content, the specific surface area and pore size of the composite gradually decreased, presumably due to the excessive CuS accumulation or deposition in the pores of CN.[50]

3.5 UV-vis DRS analysis

Light utilization plays a crucial role in photocatalytic reactions, particularly in photocatalytic CO_2 reduction reaction. The UV-vis DRS was used to study the spectral characteristics of the prepared CuS, CN, and CuS/CN composite photocatalysts, and the results are presented in Fig. 7(a). The basic absorption edge of pure CN in the visible light region is around 475 nm. In addition, CN shows

two main absorption near 265 nm and 385 nm, corresponding to the $\pi \rightarrow \pi^*$ and $n \rightarrow \pi^*$ transitions of electrons, respectively.[51] The absorption range of the CuS is relatively broad, extending from 200 nm to 600 nm, which is consistent with its inherent deep green color. Compared to CuS and CN, the absorption edge of the CuS/CN composite material is red-shifted. When the CuS loading is 15 wt%, the composite sample exhibits a maximum absorption edge at 590 nm. This may be due to the strong coupling between CuS particles and CN nanosheets, which further enhances the absorbance of the sample in the visible light region. On the other hand, the presence of CuS in the composite reduces light reflection, thereby enhancing absorption.[52] Benefiting from the further expanded light absorption range, the CuS/CN composite sample can utilize sunlight more efficiently than the CN, facilitating the separation of photogenerated electrons, and thus improving photocatalytic activity. The band gaps of CuS, CN, and 10CuS/CN were determined using the Tauc equation (eqn (1)) base on the intercept of the tangent to the plot of $(ahv)^{1/2}$ versus photon energy (hv).
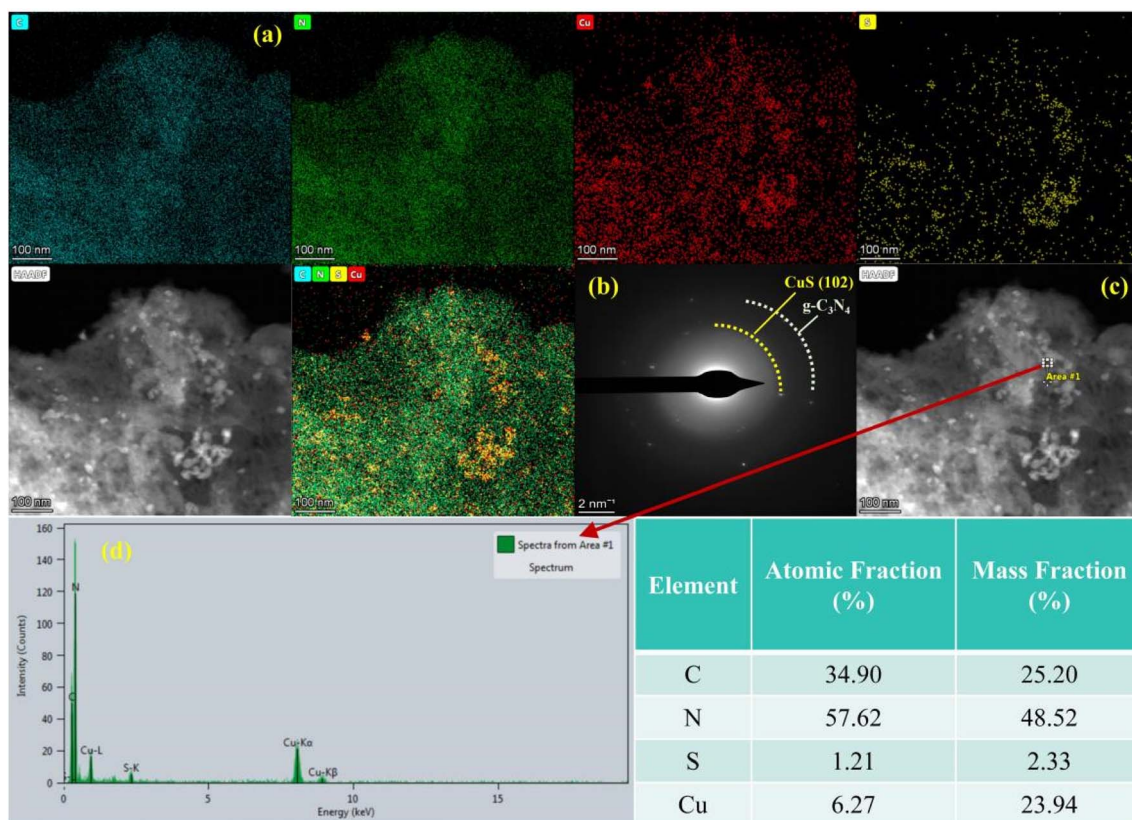
$$ahv = A(hv - E_g)^{n/2} \qquad (1)$$

Fig. 5 (a) Elemental mapping image, (b) SAED image, (c) HAADF image, and (d) EDS image of area #1 of the 10CuS/CN.

Element	Atomic Fraction (%)	Mass Fraction (%)
C	34.90	25.20
N	57.62	48.52
S	1.21	2.33
Cu	6.27	23.94

where a, v, and E_g represent the absorption coefficient, light frequency, and band gap, respectively, while A is a constant. According to previous studies, the value of n for CuS is 1 (direct semiconductor), and the value of n for CN is 4 (indirect semiconductor).[53] As shown in Fig. 7(b), the band gaps of CuS, CN, and 10CuS/CN are calculated to be 1.87 eV, 2.51 eV, and 2.02 eV, respectively. The band gap results show that the prepared samples exhibit good performance under visible light.

3.6 PL analysis

It has been reported that the photoluminescence (PL) intensity is directly correlated with the recombination rate of charge carriers.[54] Hence, PL analysis was used to study the carrier recombination in CuS, CN, and CuS/CN composite photocatalysts. Fig. 8 shows a curve of the PL intensity for all samples as a function of wavelength with an excitation wavelength of 350 nm at room temperature. All samples clearly exhibit a strong emission peak at 470 nm, which results from the
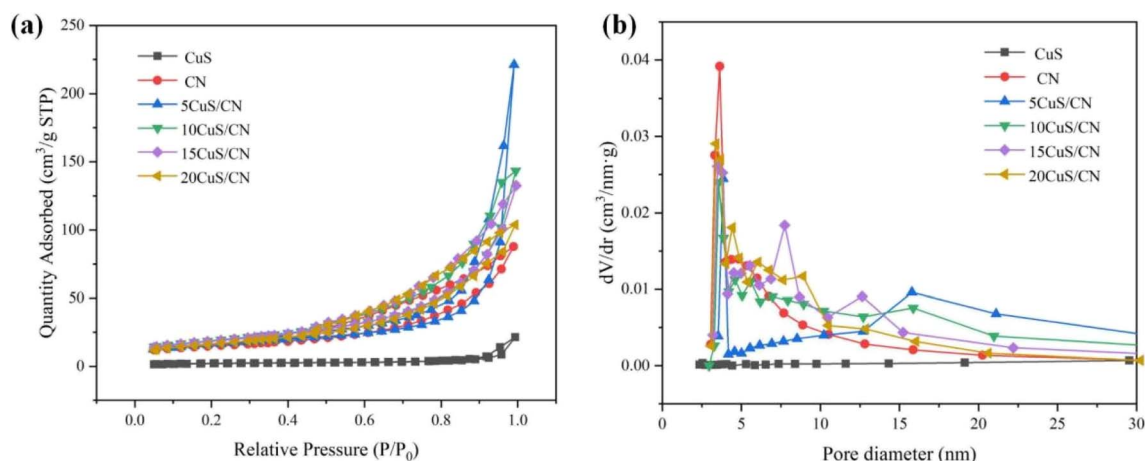

Fig. 6 (a) N$_2$ adsorption and desorption isotherms of CuS, CN, and xCuS/CN, (b) Barrett−Joyner−Halenda (BJH) pore size distribution of CuS, CN, and xCuS/CN.

Table 1 The surface properties of CuS, CN, and xCuS/CN

Materials	BET surface area ($m^2\ g^{-1}$)	Pore volume ($cm^3\ g^{-1}$)	Pore size (nm)
CuS	7.4123	0.9937	11.1970
CN	50.7652	0.9892	9.7326
5CuS/CN	54.8091	0.3419	15.4739
10CuS/CN	66.8470	0.9949	12.0520
15CuS/CN	65.7183	0.9957	10.6848
20CuS/CN	58.7256	0.9936	10.2599

recombination of photogenerated charges in CN. Notably, the PL intensity of the CuS/CN composite is significantly lower than that of pure CN. This reduction is due to the efficient facilitation of charge transfer between CN and CuS, which enhances the migration of electrons and holes. As the CuS content increases, the PL intensity initially decreases and then increases, indicating that excessive CuS loading is not always effective in reducing the carrier recombination rate. Among them, the sample loaded with 10 wt% CuS has the lowest PL intensity, suggesting that carrier recombination in 10CuS/CN is significantly suppressed. It is therefore speculated that this sample may have the best photocatalytic performance.

3.7 Photocatalytic CO_2 reduction reactions

The CO_2 photoreduction performance of the CN and CuS/CN composite photocatalyst was studied under simulated visible light. As shown in Fig. 9(a) and (b), the CN exhibited poor CO_2 photoreduction performance, and only a small amount of CO was detected on the CuS, only 8.91 μmol g^{-1}, which may be due to its smaller specific surface area and the higher recombination rate of electron–hole pairs during the reaction. After the introduction of CuS, the CO yield of the CuS/CN composite material was higher than that of pure CuS and CN, and the photocatalytic performance improved with increasing CuS loading. This is attributed to the increased specific surface area and active sites of the photocatalyst, as well as the interaction

between CuS and CN arising from the formation of a heterojunction. After 6 hours of reaction, the CO production of 10CuS/CN reached 15.34 μmol g^{-1}, which was 1.9 times and 1.7 times that of pure CN and CuS, respectively. However, with a further increase in CuS loading, the performance of the composite photocatalyst decreased slightly. This is because the reduction in the catalyst's specific surface area results in fewer active sites, and the excess CuS may also function as a recombination center for photogenerated carriers during the reaction, thereby decreasing the mobility of free charge carriers.[55]

To verify the improvement in CO_2 photocatalytic reduction performance due to the heterojunction interaction between CuS and CN, multiple groups of control experiments were conducted, as shown in Fig. 9(c). 1. CuS + CN represents the CuS and CN catalysts prepared solely by physical mixing, and its CO_2 photoreduction activity is much weaker than that of the CuS/CN composite material prepared by the hydrothermal method in this work. This reflects that the heterostructure formed by the interaction between CuS and CN significantly improves the photocatalytic performance of the single substance. Without light and the photocatalyst, almost no CO formation occurred, suggesting that both are crucial for the photocatalytic reduction of CO_2. After the reaction gas CO_2 was replaced by Ar, the CO detected in the product became negligible, proving that CO_2 was the only carbon source in the reaction process.

The stability of photocatalysts is an important indicator for evaluating their performance. The 10CuS/CN composite photocatalyst underwent three 18-hour cycle experiments under the same conditions, with the results shown in Fig. 9(d). After 18 hours of testing, although the CO yield decreased slightly, it still reached 13.35 μmol g^{-1}, about 87.6% of the initial cycle, indicating that the 10CuS/CN composite material demonstrates good cycle stability.

The material after three cycles was further characterized and analyzed. As shown in Fig. S1(a),† the crystalline phase of the XRD pattern of the sample did not change significantly after 18 h, but the intensity of the characteristic peak increased, indicating that after a long reaction time, no new species appeared in the 10CuS/CN sample, but the crystallinity of the
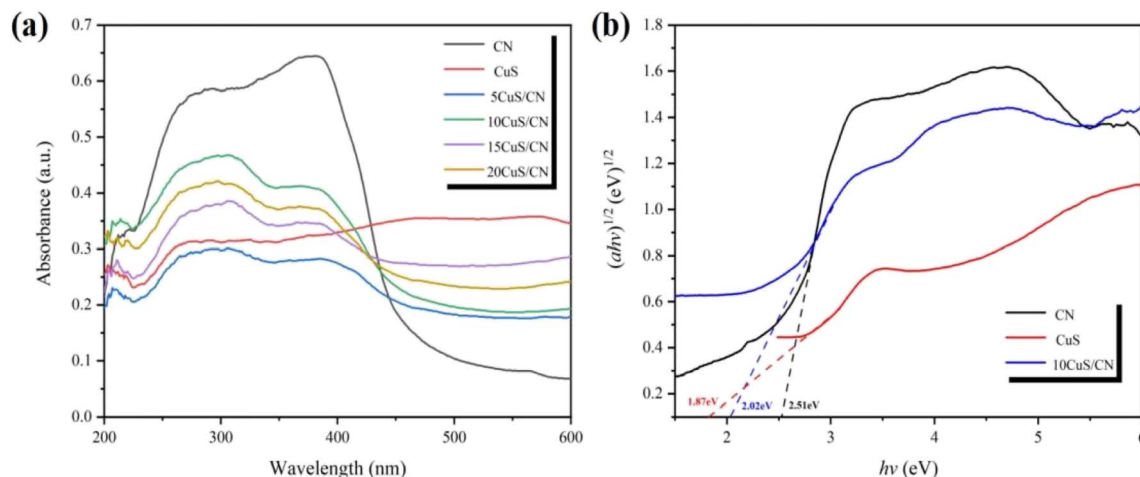

Fig. 7 (a) UV-vis DRS diffuse reflectance spectra, (b) plots of $(\alpha h\nu)^{1/2}$ vs. $h\nu$ for the band gap energy of CuS, CN and 10CuS/CN.
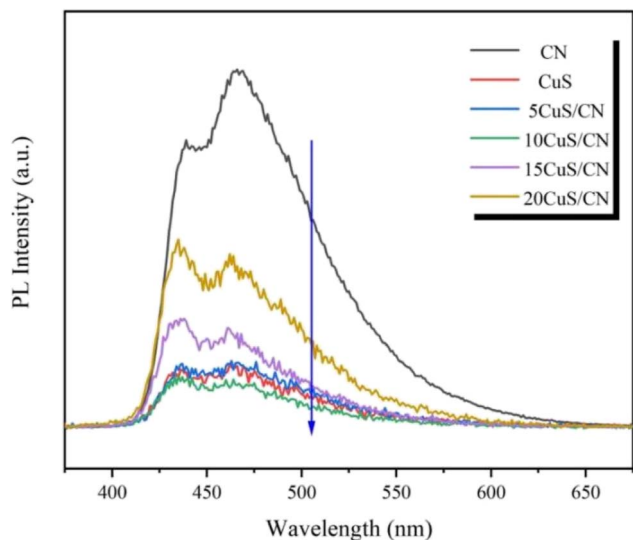
Fig. 8 Photoluminescence spectra of CuS, CN, and different wt% of CuS/CN composites.

sample increased. In addition, from the SEM of 10CuS/CN after the reaction in Fig. S1(b),† it can be seen that although the pore structure on the surface is slightly reduced, the CuS particles

can still be observed to be uniformly dispersed on the catalyst surface. Through comparing the samples before and after the reaction, it can be obtained that the crystal phase and morphology of the photocatalyst have not change significantly during the long-term photocatalytic reaction, which proved that 10CuS/CN has a good stability.

3.8 Photoelectrochemical analysis

Photocurrent (PC) and electrochemical impedance spectroscopy (EIS) measurements were performed on CN and CuS/CN composite photocatalysts to examine the improvements in charge transfer and conductivity of CN samples loaded with the CuS co-catalyst. As illustrated in Fig. 10(a), a stable photocurrent response was observed over 5 photo-switching cycles, confirming the reliable charge transfer characteristics of the prepared sample. The CuS/CN composite exhibits carrier transfer characteristics similar to those of the CN, with the 10CuS/CN sample displaying the highest photocurrent intensity. This suggests that its has the highest charge transfer efficiency, which aligns with the experimental conclusions. To further confirm the impact of composite photocatalysis on charge transfer and the suppression of photogenerated electron–hole pair recombination, EIS tests were performed, and
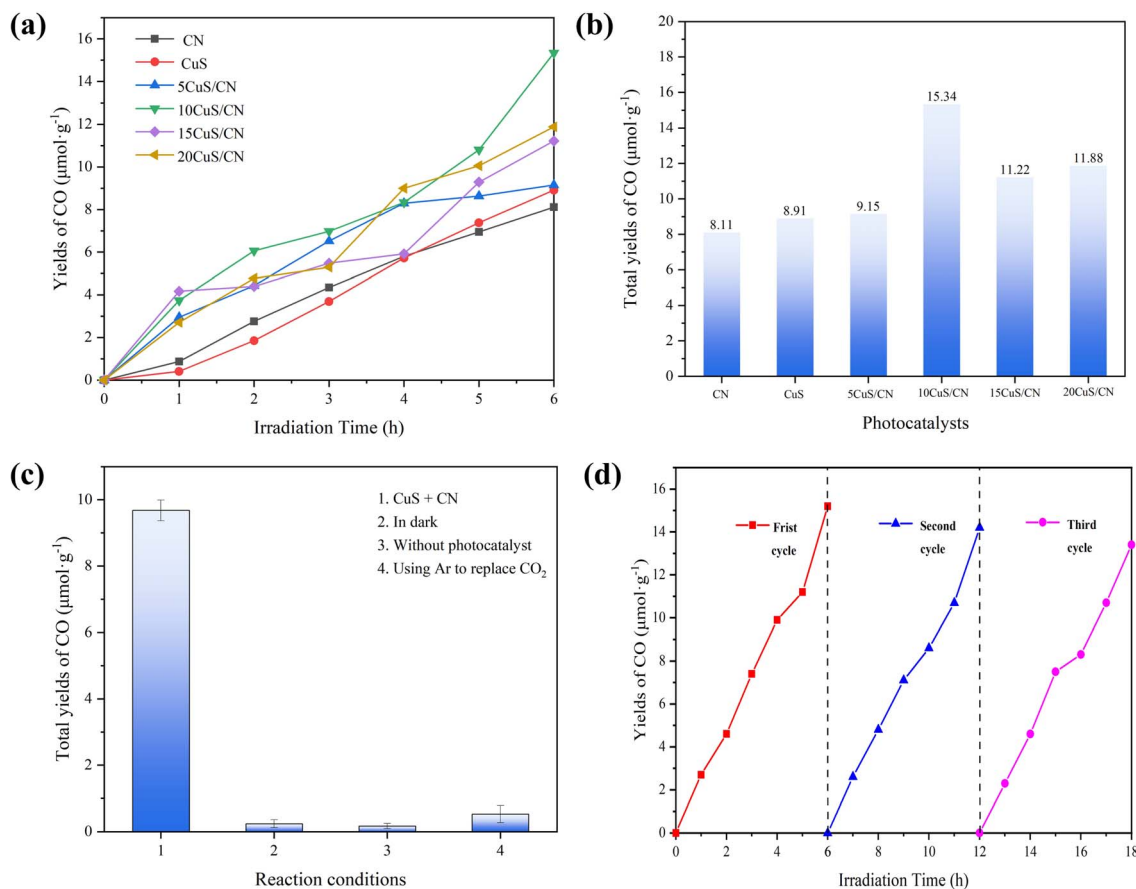

Fig. 9 (a) Photocatalytic CO_2 reduction of CN, CuS and CuS/CN samples, (b) total yield of product after 6 h irradiation, (c) CO_2 photocatalysis experiments under different conditions, (d) repeated experiments of 10CuS/CN sample. Reaction conditions: 50 mg photocatalyst, 100 mL deionized water, 100 kPa CO_2 (99.999%) 30 min, $T = 25$ °C, the photocatalytic time was 6 hours.
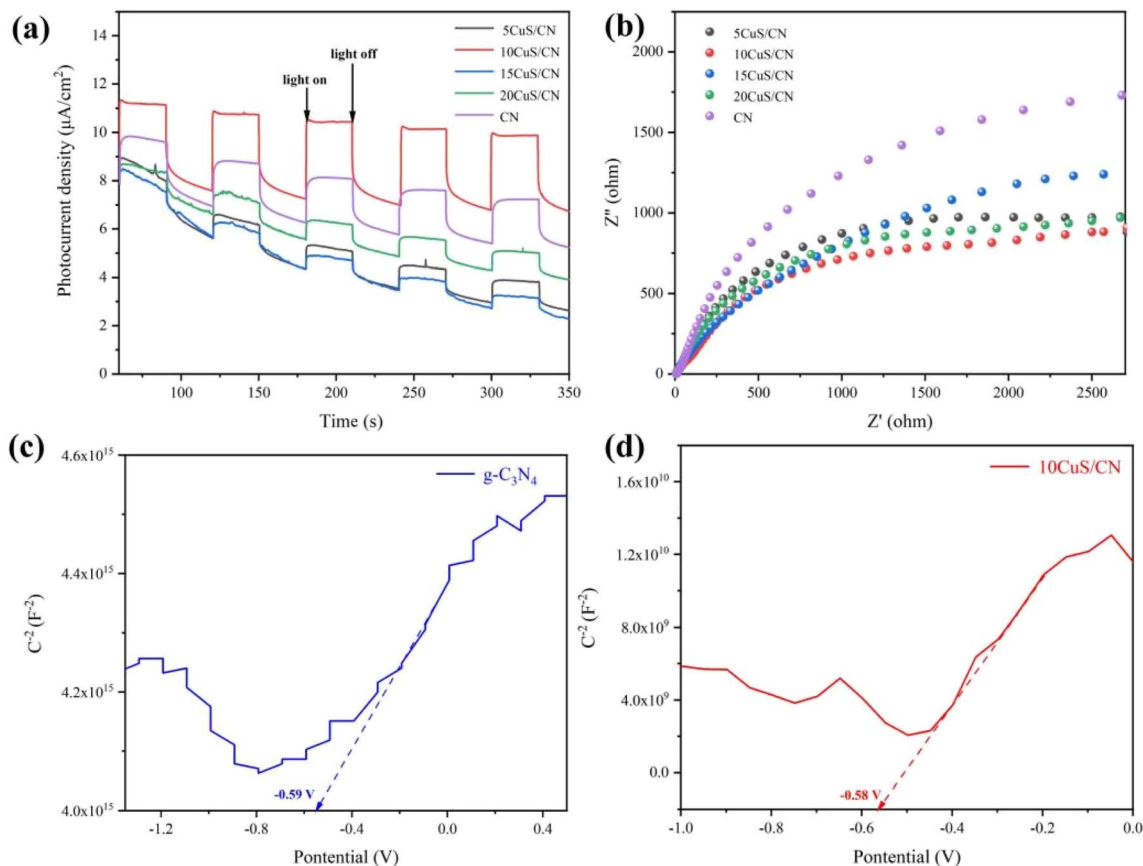
Fig. 10 (a) Photocurrent (PC), (b) electrochemical impedance spectroscopy (EIS) of CN and xCuS/CN; Mott–Schottky plots measured for (c) CN and (d) 10CuS/CN.

the results are presented in Fig. 10(b). The arc radius in the EIS Nyquist plot indicates the electron transfer rate at the interface between the working electrode and the electrolyte solution. The smaller the arc radius in the EIS graph, the lower the charge transfer resistance.[56] Compared to the CN, CuS/CN shows a smaller arc radius, suggesting that the resistance at the CuS/CN electrolyte interface is significantly lower than that at the CN/electrolyte interface, which promotes the enhancement of photocatalytic activity. Meanwhile, we also give the equivalent circuit diagram (Fig. S2†). It is noteworthy that the arc radius in the EIS graph of the 15CuS/CN and 20CuS/CN samples is larger than that of the 10CuS/CN sample. This could be attributed to the excess CuS acting as a charge recombination center, thereby reducing the electron–hole separation efficiency.

Furthermore, the electron separation kinetics of the material were investigated using time-resolved fluorescence decay spectroscopy. The decay curves of CN and 10CuS/CN composite were fitted using a double-exponential decay function (Fig. S3†), with the fitting parameters summarized in the inset. The average lifetime (τ) could be calculated by eqn (2):[57]

$$\tau = \frac{B_1\tau_1^2 + B_2\tau_2^2}{B_1\tau_1 + B_2\tau_2} \tag{2}$$

In the formula, τ_1 and τ_2 are fast and slow decay component, B_1 and B_2 are constants. The average lifetime (τ) of 10CuS/CN (8.46 ns) was significantly shorter than that of pure CN (10.63 ns),

suggesting enhanced carrier capture by active species in the composite, thereby promoting CO_2 reduction. This provides direct and quantitative evidence for the proposed IFCT mechanism. These findings demonstrate that the superior photocatalytic performance of the 10CuS/CN composite stems from the efficient separation and transport of photogenerated charge carriers.

The VB and CB values of CN, CuS and CuS/CN composites can be determined using the Mott–Schottky method. The flat-band potential of a semiconductor is typically obtained by extrapolating to $C^{-2} = 0$ at a frequency of 1000 Hz.[58] As illustrated in Fig. 10(c) and (d) and Fig. S4,† the flat-band potentials of the CN, CuS and 10CuS/CN are −0.59 V, −0.56 V and −0.58 V, respectively. Additionally, the slopes of the curves are all negative, suggesting that they are n-type semiconductors. Since the CB potential of n-type semiconductors is close to their flat-band potential, the CBs of CN, CuS and 10CuS/CN are approximately −0.59 eV, −0.56 eV and −0.58 eV, respectively.[59,60] Since the band gap energies of CN, CuS and 10CuS/CN are 2.51 eV, 1.87 eV and 2.02 eV, respectively (Fig. 7(b)), the VBs of the CN, CuS and 10CuS/CN can be calculated to be 1.92 eV, 1.31 eV and 1.44 eV, respectively, according to eqn (3).[61,62]
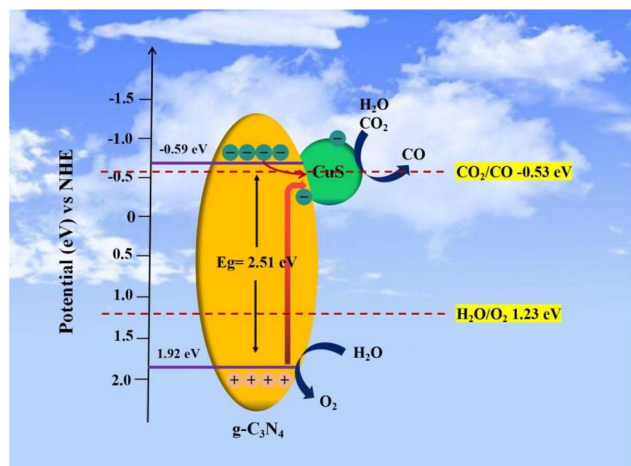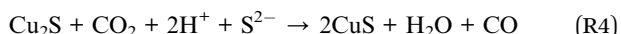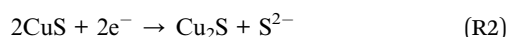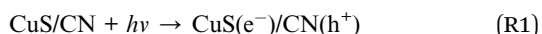
$$E_{VB} = E_g + E_{CB} \tag{3}$$

Fig. 11 Charge transfer mechanism of visible light reduction of CO_2 on CuS/CN.

Clearly, the energy band structure of the CuS/CN composite photocatalyst meets the requirements for photocatalytic reduction of CO_2.

3.9 Photocatalytic mechanism

Based on the above analysis, the energy band structure and photocatalytic mechanism of the CuS/CN composite photocatalyst are illustrated in Fig. 11. In the photoreduction of CO_2, electrons from the VB of CN are excited to the CB and subsequently transferred to the CuS co-catalyst, where they participate in the reaction with CO_2. Conversely, under simulated visible light, some electrons were directly transferred from the VB of CN to CuS, resulting in the reduction of CuS to Cu_2S and the formation of a CuS/Cu_2S mixture. The formed CuS/Cu_2S mixture can act as electron absorbers and co-catalysts, further enhancing the separation and transfer of electrons and holes, thereby improving the photocatalytic reduction of CO_2 performance.[63] The electron transfer processes involved in the CO_2 reduction reaction of the CuS/CN composite photocatalyst under illumination can be summarized as (R1)–(R4):

$$CuS/CN + hv \rightarrow CuS(e^-)/CN(h^+) \tag{R1}$$

$$2CuS + 2e^- \rightarrow Cu_2S + S^{2-} \tag{R2}$$

$$2H_2O + 4h^+ \rightarrow O_2 + 4H^+ \tag{R3}$$

$$Cu_2S + CO_2 + 2H^+ + S^{2-} \rightarrow 2CuS + H_2O + CO \tag{R4}$$

4. Conclusion

This work presents a novel g-C_3N_4 ultrathin nanosheet composite photocatalyst that is loaded with a CuS co-catalyst. The prepared composite material exhibits a larger specific surface area and better photocatalytic CO_2 reduction activity compared to the pure g-C_3N_4. The CuS loading has a great

influence on the performance of the composite photocatalyst. The experimental results indicate that the optimal CuS loading amount is 10 wt%, with the CO yield of the prepared 10CuS/g-C_3N_4 sample can reach 15.34 μmol g^{-1}, which is 1.9 times and 1.7 times that of pure g-C_3N_4 and CuS samples. In addition, CuS, as a co-catalyst, can capture electrons from the g-C_3N_4 CB, thereby suppressing the recombination of electrons and holes. On the other hand, this may be attributed to the interfacial charge transfer (IFCT) mechanism of electrons from the valence band of g-C_3N_4 to CuS, which accelerates electron–hole separation and transfer, thereby enhancing photocatalytic CO_2 reduction performance. Our results not only demonstrate the feasibility of using non-precious metal CuS as a co-catalyst for CO_2 photoreduction, but also provide a simple approach to enhance photocatalytic performance *via* light-induced IFCT.

Data availability

The data that support the findings of this study are available from the corresponding author upon reasonable request.

Conflicts of interest

There are no conflicts to declare.

Acknowledgements

References

1 M. Höök and X. Tang, *Energy Policy*, 2013, **52**, 797–809.
2 L. Gustavsson, S. Haus, M. Lundblad, A. Lundström, C. A. Ortiz, R. Sathre, N. L. Truong and P.-E. Wikberg, *Renewable Sustainable Energy Rev.*, 2017, **67**, 612–624.
3 W. Tu, Y. Zhou and Z. Zou, *Adv. Mater.*, 2014, **26**, 4607–4626.
4 X. Jiao, Z. Chen, X. Li, Y. Sun, S. Gao, W. Yan, C. Wang, Q. Zhang, Y. Lin, Y. Luo and Y. Xie, *J. Am. Chem. Soc.*, 2017, **139**, 7586–7594.
5 A. Dandia, S. L. Gupta, P. Saini, R. Sharma, S. Meena and V. Parewa, *Curr. Res. Green Sustainable Chem.*, 2020, **3**, 100039.
6 A. Dandia, D. K. Mahawar, P. Saini, S. Saini, S. L. Gupta, K. S. Rathore and V. Parewa, *RSC Adv.*, 2021, **11**, 28452.
7 A. Dandia, P. Saini, K. Kumar, M. Sethi, K. S. Rathore, M. L. Meena and V. Parewa, *Curr. Res. Green Sustainable Chem.*, 2021, **4**, 100170.
8 X.-L. Song, L. Chen, L.-J. Gao, J.-T. Ren and Z.-Y. Yuan, *Green Energy Environ.*, 2024, **9**, 166–197.
9 H. Shi, G. Chen, C. Zhang and Z. Zou, *ACS Catal.*, 2014, **4**, 3637–3643.
10 Y. Deng, J. Liu, Y. Huang, M. Ma, K. Liu, X. Dou, Z. Wang, S. Qu and Z. Wang, *Adv. Funct. Mater.*, 2020, **30**, 2002353.

11 X. Zhang, X. Yuan, L. Jiang, J. Zhang, H. Yu, H. Wang and G. Zeng, *Chem. Eng. J.*, 2020, **390**, 124475.

12 Y. Chen, L. Tan, H. Zhang, X. Zhang, Q. Chen, H. Jiang, F. Ge, S. Wei, X. Gao and P. Wang, *Res. Chem. Intermed.*, 2021, **47**, 3349–3362.

13 G. Gao, Y. Jiao, E. R. Waclawik and A. Du, *J. Am. Chem. Soc.*, 2016, **138**, 6292–6297.

14 X. Chen, J. Zhang, X. Fu, M. Antonietti and X. Wang, *J. Am. Chem. Soc.*, 2009, **131**, 11658–11659.

15 K. Kumar, P. Saini, M. Sethi, S. Saini, A. Gurjar, A. Konar, B. Dietzek-Ivansic, W. Weigand and V. Parewa, *ACS Appl. Mater. Interfaces*, 2024, **16**, 43498–43511.

16 M. Wang, G. Tana, D. Zhang, B. Li, L. Lv, Y. Wang, H. J. Ren, X. Zhang, A. Xia and Y. Liu, *Appl. Catal., B*, 2019, **254**, 98–112.

17 J. S. Santos, M. Fereidooni, V. Marquez, M. Arumugam, M. Tahir, S. Praserthdam and P. Praserthdam, *Chemosphere*, 2022, **289**, 133170.

18 X. Zhou, B. Jin, L. Li, F. Peng, H. Wang, H. Yu and Y. Fang, *J. Mater. Chem.*, 2012, **22**, 17900–17905.

19 M. Li, L. Zhang, M. Wu, Y. Du, X. Fan, M. Wang, L. Zhang, Q. Kong and J. Shi, *Nano Energy*, 2016, **19**, 145–155.

20 M. Li, L. Zhang, X. Fan, M. Wu, M. Wang, R. Cheng, L. Zhang, H. Yao and J. Shi, *Appl. Catal., B*, 2017, **201**, 629–635.

21 Q. Xu, B. Cheng, J. Yu and G. Liu, *Carbon*, 2017, **118**, 241–249.

22 Y. Peng, L. Zhou, L. Wang, J. Lei, Y. Liu, S. Daniele and J. Zhang, *Res. Chem. Intermed.*, 2019, **45**, 5907–5917.

23 Y. Zhao, M. Que, J. Chen and C. Yang, *J. Mater. Chem. C*, 2020, **8**, 16258–16281.

24 X. Han, D. Xu, L. An, C. Hou, Y. Li, Q. Zhang and H. Wang, *Appl. Catal., B*, 2019, **243**, 136–144.

25 C. Han, T. Zhang, Q. Cai, C. Ma, Z. Tong and Z. Liu, *J. Am. Ceram. Soc.*, 2019, **102**, 5484–5493.

26 Y.-F. Miao, R.-T. Guo, J.-W. Gu, Y.-Z. Liu, G.-L. Wu, C.-P. Duan and W.-G. Pan, *J. CO$_2$ Util.*, 2021, **44**, 101377.

27 Y. Zheng, J. Dong, C. Huang, L. Xia, Q. Wu, Q. Xu and W. Yao, *Appl. Catal., B*, 2020, **260**, 118220.

28 X. Lu, J. Xie, S.-Y. Liu, A. Adamski, X. Chen and X. Li, *ACS Sustain. Chem. Eng.*, 2018, **6**, 13140–13150.

29 S. Chen, M. Li, S. Yang, X. Li and S. Zhang, *Appl. Surf. Sci.*, 2019, **492**, 571–578.

30 G. Yin, M. Nishikawa, Y. Nosaka, N. Srinivasan, D. Atarashi, E. Sakai and M. Miyauchi, *ACS Nano*, 2015, **9**, 2111–2119.

31 J. Zhang, J. Yu, Y. Zhang, Q. Li and J. Gong, *Nano Lett.*, 2011, **11**, 4774–4779.

32 M. Arumugam, M. Tahir and P. Praserthdam, *Chemosphere*, 2022, **286**, 131765.

33 F. Wang, R. Wang, T. Jia, J. Wu, C. Xu, Y. Sun, X. Wang, W. Wu and Y. Qi, *J. Hazard. Mater.*, 2021, **415**, 125692.

34 F. Wang, S. Chen, J. Wu, W. Xiang and L. Duan, *Ind. Eng. Chem. Res.*, 2023, **62**, 15907–15918.

35 Y. L. Auyoong, P. L. Yap, X. Huang and S. B. A. Hamid, *Chem. Cent. J.*, 2013, **7**, 67.

36 X. Chen, H. Li, Y. Wu, H. Wu, L. Wu, P. Tan, J. Pan and X. Xiong, *J. Colloid Interface Sci.*, 2016, **476**, 132–143.

37 A. Khan, U. Alam, W. Raza, D. Bahnemann and M. Muneer, *J. Phys. Chem. Solids*, 2018, **115**, 59–68.

38 Z. Zhu, P. Huo, Z. Lu, Y. Yan, Z. Liu, W. Shi, C. Li and H. Dong, *Chem. Eng. J.*, 2018, **331**, 615–625.

39 S. Kumar, T. Surendar, A. Baruah and V. Shanker, *J. Mater. Chem. A*, 2013, **1**, 5333.

40 J. Zhang, M. Zhang, G. Zhang and X. Wang, *ACS Catal.*, 2012, **2**, 940–948.

41 Z. Chen, P. Sun, B. Fan, Q. Liu, Z. Zhang and X. Fang, *Appl. Catal., B*, 2015, **170–171**, 10–16.

42 Z. Teng, H. Lv, C. Wang, H. Xue, H. Pang and G. Wang, *Carbon*, 2017, **113**, 63–75.

43 J. Wang, T. Heil, B. Zhu, C.-W. Tung, J. Yu, H. Chen, M. Antonietti and S. Cao, *ACS Nano*, 2020, **14**, 8584–8593.

44 Q. Zhang, L. Xu, P. Ning, J. Gu and Q. Guan, *Appl. Surf. Sci.*, 2014, **317**, 955–961.

45 Y. Chen, Z. Qin, X. Wang, X. Guo and L. Guo, *RSC Adv.*, 2015, **5**, 18159–18166.

46 Y. Liao, D. Chen, S. Zou, S. Xiong, X. Xiao, H. Dang, T. Chen and S. Yang, *Environ. Sci. Technol.*, 2016, **50**, 10562–10569.

47 Y. Z. Hong, C. S. Li, G. Y. Zhang, Y. D. Meng, B. X. Yin, Y. Zhao and W. Shi, *Chem. Eng. J.*, 2016, **299**, 74–84.

48 T. Chen, C. Song, M. Fan, Y. Hong, B. Hu, L. Yu and W. Shi, *Int. J. Hydrogen Energy*, 2017, **42**, 12210–12219.

49 Z. Jiang, C. Zhu, W. Wan, K. Qian and J. Xie, *J. Mater. Chem. A*, 2016, **4**, 1806–1818.

50 M. S. Akple, J. Low, S. Wageh, A. A. Al-Ghamdi, J. Yu and J. Zhang, *Appl. Surf. Sci.*, 2015, **358**, 196–203.

51 Y. Zhou, L. Zhang, W. Huang, Q. Kong, X. Fan, M. Wang and J. Shi, *Carbon*, 2016, **99**, 111–127.

52 L. An, L. Huang, P. P. Zhou, J. Yin, H. Y. Liu and P. X. Xi, *Adv. Funct. Mater.*, 2015, **25**, 6814–6822.

53 Y. He, H. Rao, K. Song, J. Li, Y. Yu, Y. Lou, C. Li, Y. Han, Z. Shi and S. Feng, *Adv. Funct. Mater.*, 2019, **29**, 1905153.

54 U. Alam, A. Khan, W. Raza, A. Khan, D. Bahnemann and M. Muneer, *Catal. Today*, 2017, **284**, 169–178.

55 X.-Y. Dao, X.-F. Xie, J.-H. Guo, X.-Y. Zhang, Y.-S. Kang and W.-Y. Sun, *ACS Appl. Energy Mater.*, 2020, **3**, 3946–3954.

56 W. Jiang, Y. Zhao, X. Zong, H. Nie, L. Niu, L. An, D. Qu, X. Wang, Z. Kang and Z. Sun, *Angew. Chem., Int. Ed.*, 2021, **60**, 6124–6129.

57 J. Ran, T. Ma, G. Gao, X.-W. Du and S. Qiao, *Energy Environ. Sci.*, 2015, **8**, 3708–3717.

58 H. Li, H. Yu, X. Quan, S. Chen and Y. Zhang, *ACS Appl. Mater. Interfaces*, 2016, **8**, 2111–2119.

59 Y. Bai, L. Ye, T. Chen, L. Wang, X. Shi, X. Zhang and D. Chen, *ACS Appl. Mater. Interfaces*, 2016, **8**, 27661–27668.

60 D. E. Scaife, *Sol. Energy*, 1980, **25**, 41–54.

61 W. Luo, Z. Li, X. Jiang, T. Yu, L. Liu, X. Chen, J. Ye and Z. Zou, *Phys. Chem. Chem. Phys.*, 2008, **10**, 6717–6723.

62 C. Liu, Y. Zhang, F. Dong, A. H. Reshak, L. Ye, N. Pinna, C. Zeng, T. Zhang and H. Huang, *Appl. Catal., B*, 2017, **203**, 465–474.

63 M. Esmati, A. Allahresani and A. Naghizadeh, *Res. Chem. Intermed.*, 2021, **47**, 1447–1469.